Understanding NMR relaxometry of partially water-saturated rocks

O. Mohnke, R. Jorand, C. Nordlund, N. Klitzsch

Institute for Applied Geophysics and Geothermal Energy (GGE), E.ON Energy Research Center (E.ON ERC), RWTH Aachen University, Mathieustrasse 10, 52074 Aachen

Abstract

Nuclear Magnetic Resonance (NMR) relaxometry measurements are commonly used to characterize the storage and transport properties of water-saturated rocks. Estimations of these properties are based on the direct link of the initial NMR signal amplitude to porosity (water content) and of the NMR relaxation time to pore size. Herein, pore shapes are usually assumed to be spherical or cylindrical. However, the NMR response at partial water saturation for natural sediments and rocks may differ strongly from the responses calculated for spherical or cylindrical pores, because these pore shapes do not account for water menisci remaining in the corners of de-saturated angular pores. Therefore, we consider a bundle of pores with triangular cross-sections. We introduce analytical solutions of the NMR equations at partial saturation of these pores, which account for water menisci of de-saturated pores. After developing equations that describe the water distribution inside the pores, we calculate the NMR response at partial saturation for imbibition and drainage based on the deduced water distributions.

For this pore model, the NMR amplitudes and NMR relaxation times at partial water saturation strongly depend on pore shape,.i.e., arising from the capillary pressure and pore shape dependent water distribution in desaturated pores with triangular cross-sections. Even so, the NMR relaxation time at full saturation only depends on the surface-to-volume ratio of the pore. Moreover, we show the qualitative agreement of the saturation dependent relaxation time distributions of our model with those observed for rocks and soils.

1 Introduction

Understanding multi-phase flow processes in porous rocks and soils is vital for addressing a number of problems in geosciences such as oil and gas recovery or vadose zone processes, which influence groundwater recharge and evaporation. Effective permeability, which is defined as the permeability of a fluid in the presence of another fluid, is the decisive parameter for fluid transport, and depends on fluid saturation, wetting condition, and pore structure. In addition, saturation history influences the fluid content and the effective permeability (for a specific pressure), which are different for imbibition and drainage.

A method considered suitable for determining water content of rocks non-invasively is nuclear magnetic resonance (NMR), because the NMR initial signal amplitudes are directly proportional to the hydrogen content in the pore space, and the NMR relaxation times are linked to the size of the water-containing pores in the rock. In a two-phase system of water and air only the water contributes to the NMR signal response. Therefore, NMR is widely used for estimating transport and storage properties of rocks and sediments (Kenyon, 1997; Seevers 1966; Fleury et al., 2001; Arnold et al., 2006).

In recent years, several researchers have studied the relationship between NMR and multiphase flow behavior on the pore scale to better understand and infer the storage and transport properties of partially saturated rocks or sediments (e.g., Chen et al., 1994; Liaw et al. 1996; Ioannidis et al., 2006; Jia et al., 2007; Al-Mahrooqi et al., 2006; Costabel and Yaramanci, 2011, 2013; Talabi et al., 2009). As an extension of this research, we study the relationship between the water distribution inside the pores of a partially saturated rock and the system's NMR response by using bundles of pore with triangular cross-sections. While Al-Mahrooqi et al. (2006) used a similar modeling approach to infer the wettability properties in oil-water systems, this study investigates the evolution of the NMR relaxation-time spectra during drainage and imbibition. For this purpose, we consider a capillary pore ensemble that is partially saturated with water and air. Traditionally, the pores within this ensemble are assumed to have a cylindrical geometry. Depending on pressure, cylindrical capillaries are either water- or air-filled and thus they either contribute to an NMR response or not. Consequently, the NMR relaxation times of partially water-saturated capillary pore bundles always remain subsets of the fully saturated system’s relaxation-time distribution, i.e., they are a function inside the envelope of the distribution curve at full saturation (see Fig. 1). However, in porous rocks, which are formed by the aggregation of grains, the pore geometry is usually more complex (Lenormand et al., 1983; Ransohoff and Radke, 1987; Dong and Chatzis, 1995) and may exhibit angular and slit-shaped pore cross-sections rather than cylindrical capillaries or spheres (Fig. 2a). For example, in tight gas reservoir rocks Desbois et al. (2011) found three types of pore shapes that are controlled by the organization of clay sheet aggregates: i) elongated or slit-shaped, ii) triangular, and iii) multi-angular cross-sections. The relaxation-time distribution functions derived from NMR measurements for such partially saturated rocks are frequently found to be shifted towards shorter relaxation times outside the original envelope observed for a fully saturated sample, (Fig. 2b) (e.g., Applied Reservoir Technology Ltd., 1996; Bird,et al., 2005; Jaeger et al., 2009; Stingaciu, 2010a,b; Costabel, 2011).

In angular pores, water will remain trapped inside the pore corners even if the gas entry pressure is exceeded. Standard NMR pore models that assume cylindrical or spherical pore-ensembles (e.g., Kenyon, 1997), however, do not account for such residual water (2002; Tuller et al., 1999; Or and Tuller, 2000; Tuller and Or, 2001; Thern, 2014). To overcome this limitation, we adopt a NMR modeling approach initially proposed and discussed by Costabel (2011) and present numerical simulations and analytical solutions of the NMR equations for partially saturated pores with triangular cross-sections to quantify NMR signal amplitudes and relaxation times. The NMR response of a triangular capillary during drainage and imbibition depends on the water distribution inside the capillary, which is subject to pore shape and capillary pressure. Thus, in the next chapter we present the relationship between capillary pressure and water distribution inside cylindrical and triangular pore geometries during drainage and imbibition. For this purpose, the reduced similar geometry concept introduced by Mason and Marrow (1991) is used. Subsequently, based on the spatial water distribution, an analytical solution of the NMR diffusion equation (Torrey, 1956; Brownstein and Tarr, 1979) for partially saturated triangular capillaries is derived and tested by numerical simulations (Mohnke and Klitzsch, 2010). The derived equations are used to study the influence of pore size distribution and pore shape of triangular capillaries on the NMR response, in particular considering the effects of trapped water. Finally, an approach for simulating NMR signals during imbibition and drainage of triangular pore capillaries is introduced and demonstrated using synthetic pore size distributions.

2 Results and discussion

2.1 Water distribution during drainage and imbibition in a partially saturated triangular tube

In a partially saturated pore space, a curved liquid-vapor interface called the arc meniscus (AM) arises due to the pore's capillary forces. In addition, adsorptive forces between water and matrix lead to the formation of a thin water film at the rock-air interface. Such water films with a thickness typically below 20 nm (e.g., Toledo et al., 1990; Tokunaga and Wan, 1997) exhibit very short NMR relaxation times. Although water films to some extent may influence transport properties and water distribution of a partially saturated porous system (Tuller and Or, 2001), the contribution of the film volume to NMR amplitudes is very small with respect to the NMR signal amplitudes arising from the water trapped in the menisci, i.e., $V_{\mathrm{film}} \ll V_{\mathrm{meniscus}}$. Therefore, for sake of simplicity, we neglect water films in his study.

In the following discussion, we consider a triangular capillary, initially filled with a perfectly wetting liquid, i.e., contact angle $\theta = 0°$, which exhibits a constant interfacial tension σ ($\sigma_{\text{air-water}} = 73 \times 10^{-3}$ Nm^{-1} at 20°C) and is under the assumption that gravity forces are weak and therefore can be neglected. The two-phase capillary entry pressure as derived by the MS-P method (Mayer and Stowe, 1965; Princen, 1969a, b, 1970) can be expressed by the Young-Laplace equation:

$$p_{\mathrm{c}} = \frac{\sigma \cos\theta}{r_{\mathrm{AM}}} = \frac{\sigma}{r_{\mathrm{AM}}}, \qquad (1)$$

where r_{AM} is the radius of the interface arc meniscus and p_{c} is the minimum pressure difference necessary for a non-wetting phase, i.e., air, to invade a uniformly wetted (tri-)angular tube filled with a denser phase, i.e., water (see Fig. 3a). Upon consideration of a pressure difference $p > p_{\mathrm{c}}$, the non-wetting phase will begin to enter the pore and occupy the central portion of the triangle, whereas – separated by the three interface arc menisci of radius r_{AM} – the wetting fluid remains in the pore corners (Fig. 3a).

From an original triangle ABC, a new smaller triangle $A'B'C'$ of similar geometry with an inscribed circle of radius $r' = r_{\mathrm{AM}} < R_0$ can be constructed by means of the reduced similar geometry concept as introduced by Mason and Morrow (1991) (Fig. 3b). To account for different transport mechanisms during imbibition and drainage of the denser wetting phase, Mason and Morrow (1991) introduced two different principal displacement curvatures with radii r_{I} and r_{D}, respectively.

During imbibition of a (tri-)angular pore, the radius of curvature r_{AM} increases until the separate arc menisci of the corners touch and the pore fills spontaneously (“snap off”). The critical radius of curvature r_{I}, which is equal to the radius of the pore’s inscribing circle, for the angular pore at “snap-off” pressure p_{I} is then given by

$$r_{\mathrm{I}} = \frac{2A}{P}, \qquad (2)$$

According to Eq. 2, the snap-off pressure depends on the geometry of the triangle only, i.e., on its cross-sectional area A and perimeter P. In contrast, during drainage the threshold radius of curvature $r_{\mathrm{D}} = r_{\mathrm{AM}}$, at which the center of the fully saturated angular capillary spontaneously empties as the non-wetting fluid phase invades the pore, is given by

$$r_{\mathrm{D}} = P\left[\frac{1}{2G} + \left(\frac{\pi}{G}\right)^{1/2}\right]^{-1}, \tag{3}$$

with $r_{\mathrm{D}} < r_{\mathrm{I}}$ and drainage threshold pressure $p_{\mathrm{D}} > p_{\mathrm{I}}$. The dimensionless and size-independent factor $G = \frac{A}{P^2}\left(= \frac{A'}{P'^2}\right)$ reflects the shape of the triangle depending on its cross-sectional area A and perimeter P (A' and P' refer to the reduced triangle), i.e., from near-slit-shape ($\lim_{\gamma \to 0} G = 0$) to equilateral shape ($G = 0.048$). A detailed derivation of Eqs. 2 and 3 as a consequence of hysteresis between drainage and imbibition can be found in Mason and Morrow (1991).

The permeability of a porous system of such triangular capillaries is strongly influenced by the shape factor G. For single-phase laminar flow in a triangular tube the hydraulic conductance g is given by the Hagen-Poiseuille formula

$$g = k\frac{A^2 G}{\mu} \tag{4}$$

with the cross-sectional area A, the shape factor G, the fluid viscosity μ, and k, being a constant accounting for the geometrical shape of the cross-section, e.g. $k = 0.5$ for circular tubes and $k = 0.6$ for a tube with a cross-section of an equilateral triangle (Patzek and Silin, 2001). The hydraulic conductance of an irregular triangle is closely approximated by equation 1 using the same constant k as for an equilateral triangle (Øren et al., 1998). Thus, for a constant cross-sectional area the hydraulic conductance g of the pore is proportional to its shape factor G.

Combining Eqs. 1–3 with the concept of reduced similar geometry discussed above, the degree of water saturation (S_w) inside a single triangular tube with cross-sectional area A_0, perimeter P_0, and radius R_0 of its inscribing circle at a given capillary pressure p_c during imbibition and drainage can be calculated according to

$$S_{\mathrm{w}}^{\mathrm{I}}(p, A_0, P_0) = \begin{cases} 1 & , \; p_{\mathrm{c}} \leq p_{\mathrm{I}} \quad (R_0 \leq r_{\mathrm{I}}) \\ \dfrac{A_\Delta\,(\mathrm{p_c})}{A_0} & , \; p_{\mathrm{c}} > p_{\mathrm{I}} \quad (R_0 > r_{\mathrm{I}}) \end{cases} \qquad \text{(imbibition)} \tag{5}$$

$$S_{\mathrm{w}}^{\mathrm{D}}(p_{\mathrm{c}}, A_0, P_0) = \begin{cases} 1 & , \; p_{\mathrm{c}} < p_{\mathrm{D}} \; (R_0 < r_{\mathrm{D}}) \\ \dfrac{A_\Delta\,(p_{\mathrm{c}})}{A_0} & , \; p_{\mathrm{c}} \geq p_{\mathrm{D}} \; (R_0 \geq r_{\mathrm{D}}) \end{cases} \qquad \text{(drainage)} \tag{6}$$

The total area A_Δ of the triangular tube's water retaining corners, $\gamma_{1,2,3}$ (i.e., the gray areas in Figs. 4 and 5) is expressed by

$$A_\Delta\,(\mathrm{p_c}) = \sum_{i=1}^{3} A_{\gamma_i}(p_{\mathrm{c}})\,, \tag{7a}$$

where

$$A_{\gamma_{\mathrm{i}}}(\mathrm{p_c}) = \left(\frac{1}{\tan\frac{\gamma_{\mathrm{i}}}{2}} - \frac{(\pi - \gamma_{\mathrm{i}})}{2} \right) r_{\mathrm{AM}}^2(p_{\mathrm{c}}) \quad , \quad 0 < \gamma_{\mathrm{i}} < \pi \tag{7b}$$

is the area of the triangle's *i*th water-filled corner (Tuller and Or, 1999). Consequently, the total effective area A_Δ which is still occupied by water is equal to the difference between the (reduced) triangular pore area $\tilde{A}$ and the area πr_{AM}^2 of its respective inscribing circle (see Fig.

3). Above Equations 7a + b can be simplified to $A_\Delta = \left(3\sqrt{3} - \pi\right) r_{\mathrm{AM}}(p_\mathrm{c})$ if considering equilateral triangles, i.e., $\gamma_{1,2,3} = \frac{\pi}{3}$. The radius $r_{\mathrm{AM}}(p_\mathrm{c})$ of the reduced triangle's arc meniscus can be directly calculated from Eq. 1. Calculated pressure-dependent water and gas distributions during imbibition and drainage for an equilateral and arbitrary triangular capillary are shown in Figs. 4a and 5a. The corresponding water retention curves plotted in Figs. 4b and 5b illustrate the resulting hysteresis behavior of the partially saturated system and can be subdivided into three parts: at low capillary pressures, i.e., $p_\mathrm{c} < p_\mathrm{I}$, where the pore always remains fully water-saturated. For the interval $p_\mathrm{I} < p_\mathrm{c} \leq p_\mathrm{D}$, where two separate behaviors are observed: during imbibition, the water content gradually increases with increasing capillary pressure, while during drainage the pore still remains fully saturated. For pressure levels $p_\mathrm{c} \geq p_\mathrm{D}$, both drainage as well as imbibition exhibit the same gradual decrease of water saturation.

In the following section, analytical solutions for respective NMR responses that arise from partially saturated arbitrary triangular tubes are derived and matched against numerical simulations by means of the generalized differential NMR diffusion equations indroduced by Brownstein and Tarr, 1979.

2.2 NMR response for triangular capillaries

The measured NMR relaxation signal $M(t)$ is constituted by superposition of all signal-contributing pores in a rock sample (e.g., Coates et al., 1999; Dunn et al., 2002):

$$\frac{M(t)}{M_0} = \frac{1}{V_0} \sum_{i}^{N} \left(v_\mathrm{i} \times \left(1 - \mathrm{e}^{\mathrm{t} \cdot \mathrm{T}_{\mathrm{i},1}^{-1}}\right)\right), \tag{8}$$

where M_0 and V_0 are the equilibrium magnetization and total volume of the pore system, respectively. The saturated volume of the *i*th pore and its corresponding longitudinal relaxation constant are given by v_i and $T_{i,1}$, respectively.

Following derivations of Brownstein and Tarr (1979), the inverse of the longitudinal relaxation time T_1 is linearly proportional to the surface-to-volume ratio of a pore according to

$$T_1^{-1} = T_{1B}^{-1} + \rho_s \frac{S_a}{V}, \tag{9}$$

where T_{1B} is the bulk relaxation time of the free fluid and ρ_s is the surface relaxivity, a measure of how quickly protons lose their magnetization due to magnetic interactions with paramagnetic impurities and reduced correlation times at the fluid-solid interface, which can be attributed to paramagnetic ions at mineral grain surfaces. V and S_a are the pore's volume and active surface boundaries, respectively. In this context, an active boundary refers to an interfacial area, i.e., the pore wall, where $\rho_s > 0$ and, thus, enhanced NMR relaxation will occur as the molecules diffuse at the pore walls. This model, however, is based on the general assumption of a relaxation regime that is dominated by surface relaxation processes (*fast diffusion*), i.e., the fluid molecules move sufficiently fast and thus explore all parts of the pore volume several times with respect to the time scale (~T_1) of the experiment.

Upon consideration of a long (triangular) capillary, its surface-to-volume-ratio equals its perimeter-to-cross-section-ratio, i.e., $S/V = P/A$. Consequently, Eq. 9 can be written as

$$T_1^{-1} = T_{1B}^{-1} + \rho_s \frac{P_0}{A_0}, \tag{10}$$

where P_0 is the saturated tube's (active) perimeter and A_0 its cross-sectional area for a circular cross-section, $\frac{P_0}{A_0} = \frac{2}{r_0}$, with r_0 being the capillary radius. Hence, the relaxation rate of a fully saturated arbitrary triangular pore *ABC* can be expressed in terms of its shape factor *G* and perimeter P_0:

$$T_1^{-1} = T_{1\mathrm{B}}^{-1} + \frac{\rho_s}{G\,P_0}\left(= T_{1\mathrm{B}}^{-1} + \rho_s \frac{L_{\mathrm{AB}} + L_{\mathrm{BC}} + L_{\mathrm{CA}}}{L_{\mathrm{AB}} L_{\mathrm{CA}} \sin(\gamma_{\mathrm{A}})}\right) \quad , \tag{11}$$

where $\mathrm{L_{AB}}$, $\mathrm{L_{BC}}$, and $\mathrm{L_{AC}}$ are the lengths of a triangle's sides and γ_{A} is the angle at corner A (see Fig. 3). As illustrated in Fig. 6, the relaxation times of a fully saturated pore decrease with decreasing pore shape factor G – and thus, decreasing hydraulic conductance – and increasing pore perimeter P. By reducing one angle from 60° to 0° while fixing another at 60°, we increase P/A for a constant cross-sectional area A. In the special case of an equilateral triangular capillary, i.e., $P_0/A_0 = \frac{12}{\sqrt{3}\,\mathrm{L}_0}$, Eq. 11 can be simplified to

$$T_1^{-1} = T_{1\mathrm{B}}^{-1} + \rho_s \frac{12}{\sqrt{3}\,\mathrm{L}_0} . \tag{12}$$

Now we consider the previously discussed water-air system of a partially saturated equilateral triangular capillary. Here, the NMR signal will originate from the water retained at the corners. Replacing A_0 in Eq. 10 with an effective area A_γ or A_Δ as derived by Eqs. (7a) and b, respectively. A_Δ reflects the actual pore fraction that contributes to the NMR signal, i.e., the portion of the pore area A_0 that still remains occupied by water.

Supposing the air-water interface to be a passive boundary with respect to NMR surface relaxivity, i.e., $\rho_s = 0$, the effective active boundary is exclusively controlled by the pore wall segments ($\rho_s > 0$) in contact with water (wetting phase) (Fig. 7). Thus, the active perimeter of such a partially saturated triangular capillary is equal to its pressure-dependent reduced triangle's perimeter, $P'_\Delta\left(r^{\mathrm{I,D}}(p_c)\right)$, according to

$$P_\Delta = \sum_{i=1}^{N=3} P_{\gamma_{\mathrm{i}}} \ , \tag{13}$$

with

$$P_{\gamma_\mathrm{i}} = 2\frac{r_{\mathrm{AM}}(p_\mathrm{c})}{\tan\frac{\gamma_\mathrm{i}}{2}} \quad , \quad 0 < \gamma_\mathrm{i} < \pi \tag{14}$$

being the perimeter of the *i*th water-filled corner. Consequently, the NMR relaxation rates and NMR signal (amplitude) evolution during drainage and imbibition of a single equilateral triangular capillary can be expressed by

$$T_{\Delta,1}^{-1} = \begin{cases} T_{1\mathrm{B}}^{-1} + \rho_s \dfrac{P_0}{A_0} & , \quad S_\mathrm{w}^{\mathrm{I,D}} = 1 \\[2ex] T_{1\mathrm{B}}^{-1} + \rho_s \dfrac{P_\Delta^{\mathrm{I,D}}(p_\mathrm{c}, A_0, P_0)}{A_\Delta^{\mathrm{I,D}}(p_\mathrm{c}, A_0, P_0)} & , \quad S_\mathrm{w}^{\mathrm{I,D}} < 1 \end{cases} \tag{15}$$

and

$$\frac{m(t)}{m_0} = S_\mathrm{w}^{\mathrm{I,D}}(p_\mathrm{c}, A_0, P_0)\left(1 - \mathrm{e}^{\frac{-\mathrm{t}}{\mathrm{T}_{\Delta,1}}}\right), \tag{16}$$

respectively. Fig. 8 illustrates the pressure-dependent water distribution inside a single equilateral triangular capillary (with a side length of 1 μm) during drainage (a) and evolution of longitudinal magnetization (b). As the water saturation is reduced with increasing pressure, both NMR amplitudes and relaxation times (c) decrease. Note that only a single characteristic relaxation time at each saturation degree is observed, since each corner has the same P_γ/A_γ, and consequently the same T_1 value.

In contrast, each water-filled corner of a partially saturated non-equilateral triangle, i.e., $\gamma_1 \neq \gamma_2 \neq \gamma_3$, can have a different P_γ/A_γ ratio, and thus will show a different relaxation time and amplitude. As a result, depending on its individual shape, even a single partially saturated pore exhibits a multi-exponential NMR relaxation behavior based on Eq. (8) according to

$$\frac{m(t)}{m_0} = \frac{1}{A_0}\sum_{i=1}^{N=3} A_{\gamma_\mathrm{i}}^{\mathrm{I,D}}\left(1 - \mathrm{e}^{\frac{-\mathrm{t}}{\mathrm{T}_{\gamma_\mathrm{i},1}}}\right), \tag{17}$$

with $T_{\gamma_{i,1}} = \frac{1}{T_{1B}} + \rho_s \frac{P_{\gamma_i}}{A_{\gamma_i}}$ and $\frac{A_{\gamma_i}^{I,D}}{A_0}$ being the characteristic relaxation time and amplitude contribution of the *i*th corner of the triangle, respectively. Figure 9 exemplifies such different multi-exponential relaxation behavior for a pore with a right triangle geometry with angles of $(\gamma_1 = 30°, \gamma_2 = 60°, \gamma_3 = 90°)$ and the same cross-sectional area as the equilateral pores in Fig. 8 (i.e., ~ NMR porosity).

To test the analytical (fast diffusion) models for partially saturated triangular capillaries derived above, the calculated longitudinal NMR relaxation times and amplitudes are compared to solutions obtained from 2D numerical simulations of the general NMR diffusion equation (Mohnke and Klitzsch, 2010):

$$\dot{m} = \left(\mathrm{D}\nabla^2 - \frac{1}{T_\mathrm{B}}\right) m\,, \tag{18}$$

with normalized initial values $m(\boldsymbol{r}, t = 0) = \frac{M_0 = 1}{A}$ and boundary conditions

$$D\boldsymbol{n}\nabla m\Big|_\mathrm{P} = \rho_s m\Big|_\mathrm{P}\,, \tag{19}$$

where m is the magnetization density, D the diffusion coefficient of water, T_B the bulk relaxation time, ρ_s the interface's surface relaxivity, $\boldsymbol{n}$ the outward normal, and A and P the pore's cross-sectional area and perimeter, respectively. To demonstrate the consistency of the introduced model with numerical results obtained by Mohnke and Klitzsch (2010), above equations were solved numerically using finite elements to simulate the respective NMR relaxation data of the studied triangular geometries.

As shown in Fig. 10, analytically (+) calculated NMR relaxation data for drainage and imbibition for an equilateral triangular pore are in a very good agreement ($R^2 > 0.99$) with data obtained from numerical simulations (o).

The model was also matched against numerical simulations for pores with arbitrary angles. Figure 11 illustrates 2D finite elements simulations using saturated pore corners with angles γ_{i} ranging from 5° to 175° with equal active surface-to-volume ratios $P_{\gamma_{\mathrm{i}}} / A_{\gamma_{\mathrm{i}}} = const.$ and thus $T_{1,\mathrm{i}} = const.$ The simulations were compiled and compared to their respective analytical solutions. The ratios of the numerical to the analytical model results for NMR amplitudes, i.e., NMR signal amplitudes, A_{γ}, and relaxation times, $T_{1,\gamma}$ as function of corner aperture γ are shown and confirm a near perfect correlation of $R^2 > 0.99$, with deviations generally less than 0.05 %. In this regard, the slight increase in divergence of relaxation time ratios at acute and obtuse angles can be attributed to numerical errors resulting from a decrease of the finite element's grid quality due to extremely high or low x-to-y ratios at these apertures. The above model is applicable to any angular capillary geometry, such as square or octahedron.

2.3 Simulated water retention curves and NMR relaxation data of partially saturated pore distributions

The goal of this section is to evaluate how pore shape affects the forward-modeled NMR response of a partially saturated system of pores (a pore size distribution). As discussed earlier, the NMR relaxation time of a single water-filled capillary pore is inversely proportional to its surface-to-volume-ratio. Thus, at full water saturation the relaxation-time distribution obtained from a multi-exponential NMR relaxation signal represents the pore-size distribution of the rock. At partial water saturation it is often assumed that the NMR relaxation signal still represents the pore size distribution of the water saturated pores (e.g., Stingaciu, 2010b). We are going to demonstrate that this is valid for cylindrical but not for (tri-) angular pores.

In contrast to cylindrical pores, capillaries with (tri-)angular cross-sections may be partially water-saturated during drainage or imbibition (cf. Fig. 8 and 9) because of the water remaining in the corners. Thus, they show a different water retention behavior and the "desaturated" pores, i.e. their arc menisci, contribute to the NMR signal. Consequently, with increasing pressure (i.e. decreasing water saturation) the NMR relaxation behavior of the partially water-saturated triangular capillary pore bundle successively shifts to signal contributions with shorter relaxation times, exceeding the original distribution at full saturation. This shift reflects the fast relaxation of residual water trapped in the pore corners (Figure 12). This behavior in angular pore geometries is demonstrated in Figure 13. Here, the NMR relaxation components for a fully (blue line) and partially saturated (red and green) distribution of triangular capillaries are plotted. The green and red peaks show the signals of the residual water in the pore corners. As a consequence of reduced geometry concept the remaining water in the corners can be considered similar in size and shape due to the same NMR relaxation time and thus only depends on pressure and not on pore size. Therefore with decreasing saturation, i.e., increasing pressure, the NMR signal of the arc menisci increases and shifts towards smaller relaxation times. If the non-wetting phase (air) has entered all capillaries, only one single relaxation time remains for the pore bundle of equilateral triangles. For arbitrarily shaped triangular pores, three relaxation times would remain for the de-saturated pore system. Hence, the concept of a relaxation time distribution assumed in conventional NMR inversion and interpretation approaches would be no longer valid.

We applied the concept of fitting multi-exponential relaxation time distributions to NMR transients calculated for pore bundles of circular and equilateral triangle cross-sections in order to study how pore shape affects the typically-shown relaxation time distributions.

Water drainage and imbibition with water as wetting and air as the non-wetting fluid were investigated by simulating water retention curves and corresponding NMR relaxation signals for a log-normal distributed pore size ensemble as shown in Figure 14.

Herein, to clarify the subsequent discussion we focused only on the equilateral triangalar capillary model. Other angular pore shapes (e.g., right angular triangles or squares) will exhibit a similar behavior. Capillary pressure curves presented in Figure 15a were calculated from Eq. 1, 5, and 6 for pore bundles with circular and equilateral triangle cross-sections. In contrast to water retention curves calculated for the cylindrical capillary model significant hysteresis between drainage and imbibition can be observed for the triangular capillary model, i.e. in terms of initial amplitudes (=saturation) and respective mean relaxation times (Figure 15b). Corresponding NMR T_1 relaxation (saturation recovery) signals shown in Figure 15c,d and e were calculated using a uniform surface relaxivity of $\rho_s = 10\ \mu\mathrm{m/s}$ and a water bulk relaxation $T_{1,bulk} = 3\ s$.

The NMR T_1 relaxation signals were simulated for 20 saturation levels of the drainage and imbibition curves ranging from S = 100% to S < 1% water saturation. The corresponding relaxation time distributions (Figure 15f-h) of the NMR T_1 transients were determined by means of a regularized multi-exponential fitting using a nonlinear least squares formulation solved by the Levenberg-Marquardt approach (e.g., Marquardt, 1963; Mohnke, 2010). Inverse modeling results of NMR data calculated for the drainage branches using the cylindrical capillary bundle (Fig. 15f) exhibit a shift of the distribution’s maximum towards shorter relaxation times with decreasing saturation (i.e., increasing pressure). As anticipated, the derived distribution functions remain inside the envelope of the relaxation-time distribution curve at full saturation (see also Fig. 1a).

In contrast, inversion results for equilateral triangular capillary ensembles (Fig. 15f-h) – both for imbibition and drainage – show a similar shift to shorter relaxation times with decreasing saturation but also shift towards the outside the initial distribution at full saturation due to NMR signals originating from trapped water in the pore corners of the desaturated triangular capillaries. The effect of the pore corners on relaxation times at low saturations is also recognizable when comparing the (geometric) mean relaxation times, normalized on the values observed at full saturation (Fig. 15b): Both, the drainage and the imbibition hysteresis branch of the triangular pore bundle show smaller mean relaxation times than the cylindrical pore bundle.

In conclusion, the calculated inverse models for the triangular capillary bundle qualitatively agree with the behavior of the inverted NMR relaxation-time distributions at partial saturation that are frequently observed in experimental data, e.g., of the Rotliegend sandstone shown in Fig. 2.

3 Summary and conclusions

Experimental NMR relaxometry data and corresponding relaxation-time distributions obtained at partial water/air saturation were explicated by a modification of conventional NMR pore models using triangular cross-sections. The derived analytical solutions for calculating surface-dominated (fast diffusion) NMR relaxation signals in fully and partially saturated arbitrary angular capillaries were consistent with respective results obtained from numerical simulations of the general NMR diffusion equations.

Shape and size of triangular pores can strongly influence both NMR amplitudes and decay time distribution and the rock's flow properties, i.e., saturation and (relative) permeability. At full saturation the NMR relaxation time depends on the surface-to-volume ratio, which in turn depends on shape if considering angular pore capillaries. However, at partial saturation, the pore shape even more strongly influences the water distribution inside the pore system, and thus the NMR signal. In contrast to cylindrical capillaries, angular capillaries also contribute to the NMR signal even after desaturation of the pore due to the water remaining in the pore corners.

In this regard, non-equilateral triangular capillaries at partial saturation exhibit a three-exponential relaxation behavior due to different perimeter-to-surface (= surface-to-volume) ratios of the water in the pore corners whereas the relaxation time of the trapped water in the corners depends on pressure and not on pore size. Therefore, it can be noted that the NMR signal at partial saturation is affected by both the surface-to-volume ratio of the water saturated and the pore shapeof the desaturated pores .

Moreover, we studied the NMR response of a triangular pore bundle model by jointly simulating the water retention curves for drainage and imbibition and the corresponding NMR T_1 relaxometry data. With decreasing water saturation, the simulated NMR relaxation distributions shift towards shorter relaxation times below the initial distribution enveloped at full saturation, which is principally in agreement with the relaxation behavior observed in experimental NMR data from rocks (e.g., Figure 2b).

Ongoing research will include further experimental validation and implementation of the introduced approach in an inverse modeling algorithm for NMR data obtained from partially saturated rocks to predict absolute and relative permeability at laboratory and borehole scales. Without considering angular pores the NMR signal of trapped water cannot be explained, i.e., using the classical approach of circular capillaries one cannot find a pore size distribution which explains the relaxation time distributions at all saturations sufficiently (e.g., Mohnke, 2014). On the other hand, angular pore models can account for the trapped water and thus overcome the limitation of the classical approach. Moreover, following the approach of Mohnke (2014) but considering angular pores we strive for estimating surface relaxivity, pore size distribution, and pore shape by jointly inverting NMR data at different saturations. Based on the obtained pore size distribution and triangle shape we expect to improve the prediction of the absolute and relative permeabilities considerably.

Acknowledgements

The study was supported by the German Research Foundation (DFG) in the framework of the Transregional Collaborative Research Centre 32 (SFB TR 32) and Wintershall AG in the framework of Wintershall Tight Gas Consortium at RWTH Aachen University.

References

Al-Mahrooqi, S. H., Grattoni, C. A., Muggeridge A. H., Zimmermann, R. W., and Jing, X. D.: Pore-scale modelling of NMR relaxation for the characterization of wettability, J. Petrol. Sci. Eng., 52, 172–186, 2006.

Applied Reservoir Technology Ltd.: The NMR Sandstone Rock Catalogue, Long Melford, Suffolk, U.K., 1996.

Arnold, J., Clauser, C., Pechnig, R., Anferova, S., Anferov, V., and Blümich, B.: Porosity and Permeability from Mobile NMR Core-Scanning, Petrophysics, 47, 306–314, 2006.

Bird, N.R.A., Preston, A. R., Randall, E. W., Whalley ,W.R. and Whitmore, A.P..: Measurement of the size-distribution of water-filled pores at different matric potentials by STRAFI-NMR relaxation-time measurements. European Journal of Soil Science. 56: 135-143, 2005.

Brownstein, K., and C. Tarr, C. (1979), Importance of classical diffusion in NMR studies of water in biological cells, Phys. Rev. A, 19, 2446–2453, 1979.

Chen, S., Liaw, H. K., and Watson, A. T.: Measurements and analysis of fluid saturation-dependent NMR relaxation and linebroadening in porous media, Magn. Reson. Imaging, 12(2), 201–202, 1994.

Coates, G. R., Xiao, L., and, Prammer, M. G.: NMR Logging Principles and Applications, Halliburton Energy Services, Houston, TX, 234 pp., 1999.

Costabel, S.: Nuclear magnetic resonance on laboratory and field scale for estimating hydraulic parameters in the vadose zone, PhD thesis, Berlin University of Technology, 2011. (opus4.kobv.de/opus4-tuberlin/files/3173/costabel_stephan.pdf)

Costabel, S. and Yaramanci, U.: Relative hydraulic conductivity in the vadose zone from magnetic resonance sounding - Brooks-Corey parameterization of the capillary fringe, Geophysics, 76(3), G61–G71, doi:10.1190/1.3552688, 2011.

Costabel, S. and Yaramanci, U.: Estimation of water retention parameters from nuclear magnetic resonance relaxation time distributions, Water Resour. Res., 49(4), 2068–2079, doi:10.1002/wrcr.20207, 2013.

Desbois, G., Urai, J. L., Kukla, P. A., Konstanty, J., and Baerle, C.: High-resolution 3D fabric and porosity model in a tight gas sandstone reservoir: A new approach to investigate microstructures from mm- to nm-scale combining argon beam cross-sectioning and SEM imaging, J. Petrol. Sci. Eng., 78, 243–257, doi:10.1016/j.petrol.2011.06.004, 2011.

Dong, M. and Chatzis, I.:, The imbibition and flow of a wetting liquid along the corners of a square capillary tube, J. Colloid Interface Sci., 172, 278–288, 1995.

Dunn K. J., Bergman D. J., and LaTorraca G. A.: Nuclear Magnetic Resonance: Petrophysical and Logging Applications, Pergamon: Elsevier Science, Amsterdam, 2002.

Fleury, M., Deflandre F., and Godefroy, S.: Validity of permeability prediction from NMR measurements, CR. Acad. Sci. Series IIC – Chemistry, 4, 869–872, doi:10.1016/S1387-1609(01)01343-3, 2001.

Ioannidis, M., Chatzis, I., Lemaire, C., and Perunarkilli, R.: Unsaturated hydraulic conductivity from nuclear magnetic resonance measurements, Water Resour. Res., 42(7), W07201, 6 pages, doi:10.1029/2006WR004955, 2006.

Jaeger, F., Bowe, S., van As, H., and Schaumann, G. E. (2009). Evaluation of 1 H NMR relaxometry for the assessment of pore size distribution in soil samples. European Journal of Soil Science, 60:1052 – 1064.

Jia, P., Dong, M., and Dai, L.: Threshold pressure in arbitrary triangular tubes using RSG concept for all wetting conditions, Colloid. Surface A, 302, 88–95, 2007.

Kenyon, W.: Petrophysical principles of applications of NMR logging, Log Anal. 38(2), 21–43, 1997.

Lenormand R., Zarcone C., Sarr, A.: A Mechanisms of the displacement of one fluid by another in a network of capillary ducts, J. Fluid Mech., 135, 337–353, 1983.

Liaw, H.-K., Kulkarni, R., Chen, S., and Watson, A.T.: Characterization of fluid distributions in porous media by NMR techniques, AIChE J., 42(2), 538–546, doi: 10.1002/aic.690420223, 1996.

Marquardt, D. W.: An Algorithm for the Least-Squares Estimation of Nonlinear Parameters, Siam J. Appl. Math., 11(2), 431–441, 1963.

Mason, G. and Morrow, N. R.: Capillary behavior of a perfectly wetting liquid in irregular triangular tubes, J. Colloid. Interf. Sci., 141, 262–274, 1991.

Mayer, R. P., and Stowe, R. A.: Mercury porosimetry-breakthrough pressure for penetration between packed spheres, J. Colloid. Interf. Sci., 20, 893–911, 1965.

Mohnke, O.: Improved forward and inverse modelling of Surface NMR relaxation signals using multi-exponential decomposition, Ph.D. thesis, Technical University Berlin, Berlin, 2010.

Mohnke, O. and Klitzsch, N.: Microscale Simulations of NMR Relaxation in Porous Media Considering Internal Field Gradients, Vadose Zone J., 9, 846–857, doi:10.2136/vzj2009.0161, 2010.

Øren, P. E., S. Bakke, and O. J. Arntzen, Extending predictive capabilities to network models, SPE Journal, 3, 324-336, 1998.

Or, D. and Tuller, M.: Flow in unsaturated fractured porous media: Hydraulic conductivity of rough surfaces. Water Resour. Res., 36(5), 1165–1177, doi:10.1029/2000WR900020, 2000.

Patzek, T. W., and D. B. Silin, Shape factor and hydraulic conductance in noncircular capillaries I. One-phase creeping flow, Journal of Colloid and Interface Science, 236, 295-304, 2001.

Princen, H. M.: Capillary phenomena in assemblies of parallel cylinders I. Capillary rise between 2 cylinders, J. Colloid. Interf. Sci., 30, 69–75, 1969a.

Princen, H. M.: Capillary phenomena in assemblies of parallel cylinders II. Capillary rise in systems with more than 2 cylinders, J. Colloid. Interf. Sci., 30, 359–371, 1969b.

Princen, H. M.: Capillary phenomena in assemblies of parallel cylinders III. Liquid columns between horizontal parallel cylinders, J. Colloid. Interf. Sci., 34, 171–184, 1970.

Ransohoff, T. C., and Radke, C. J.: Laminar flow of a wetting liquid along the corners of a predominantly gas-occupied noncircular pore, J. Colloid Interface Sci., 121, 392–401, 1987.

Seevers, D. O.: A nuclear magnetic method for determining the permeability of sandstones, Society of Professional Well Log Analysts, vol. 6, paper L, Housten, Texas, 1966.

Stingaciu, L. R.: Characterization of natural porous media by NMR and MRI techniques: High and low magnetic field studies for estimation of hydraulic properties, Ph.D. thesis, RWTH Aachen, URL: http://darwin.bth.rwth-aachen.de/opus3/volltexte/2010/3392/, 2010a (accessed on 06/30/2014).

Stingaciu, L. R., Weihermüller, L., Haber-Pohlmeier, S., Stapf, S., Vereecken, H., and Pohlmeier, A.: Determination of pore size distribution and hydraulic properties using nuclear magnetic resonance relaxometry: A comparative study of laboratory methods. Water Resour. Res., 46, 1–11, doi:10.1029/2009WR008686, 2010b.

Talabi, O., AlSayari, S. Iglauer, I., and Blunt, J.: Pore-scale simulation of NMR response, J. Petrol. Sci. Eng., 67, 168–178, 2009.

Thern, H.: Examining the fluid film model in porous media by NMR rock catalogue data, Symposium of the Society of Core Analysts, Avignon, France, paper SCA2014-051.

Tokunaga, T. K. and Wan, J.: Water film flow along fracture surfaces of porous rock, Water Resour. Res., 33(6), 1287–1295, doi:10.1029/97WR00473, 1997.

Toledo, P. G., Novy, R. A., Davis, H. T., and Scriven, L. E.: Hydraulic Conductivity of Porous Media at Low Water Content, Soil Sci. Soc. Am. J., 54, 673–679, 10.2136/sssaj1990.03615995005400030007x, 1990.

Torrey, H. C.: Bloch equations with diffusion terms, Phys. Rev., 104(3), 563–565, doi:10.1103/PhysRev.104.563, 1956.

Tuller, M., Or, D., and Dudley, L.M.: Adsorption and capillary condensation in porous media - liquid retention and interfacial configurations in angular pores, Water Resour. Res., 35(7), 1949–1964, doi: 10.1029/1999WR900098, 1999.

Tuller, M. and Or, D.: Hydraulic conductivity of variably saturated porous media: Film and corner flow in angular pore space, Water Resour. Res., 37(5), 1257–1276, DOI: 10.1029/2000WR900328, 2001.

FIGURES

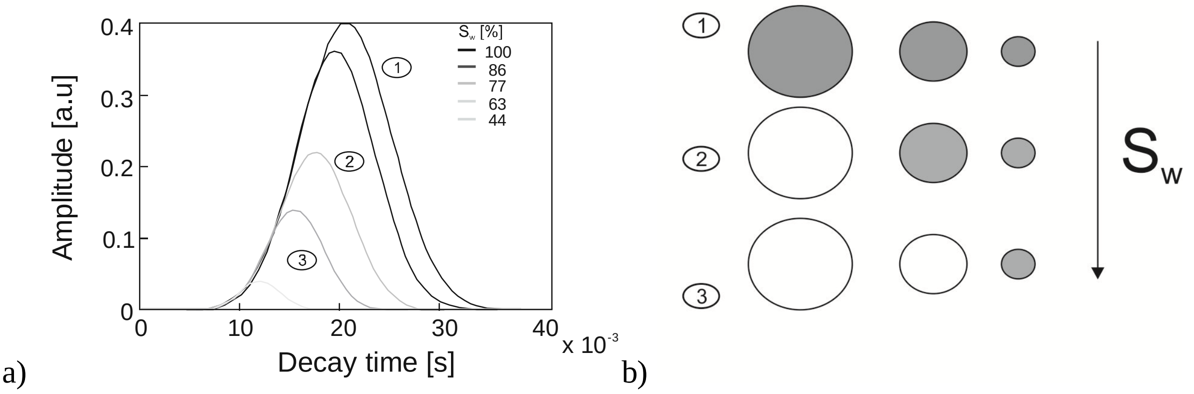

Figure 1. a) NMR decay time distributions at different water saturation levels for a classical cylindrical capillary pore distribution. b) Concept sketch of saturated (gray) and de-saturated capillaries, e.g., during drainage.

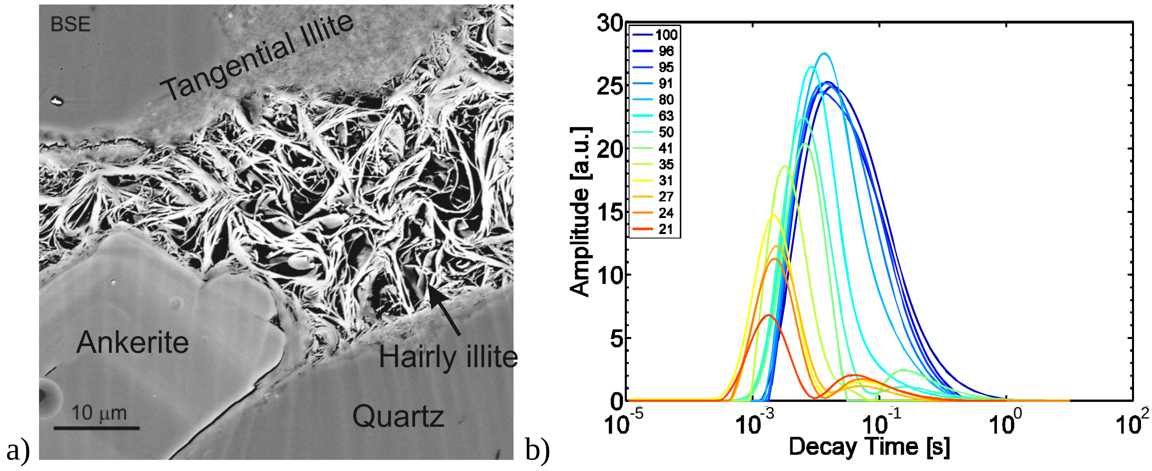

Figure 2. a) Complex pore structure of a Rotliegend tight gas sandstone. Pore spaces are filled with tangential and hairly illite and exhibit different pore types with elongated or slit-shaped, triangular, and multi-angular cross-sections. b) T_1 decay time distributions calculated from inverse Laplace transform performed on Rotliegend sandstone (porosity 13%, permeability 0.1 mD) at different water saturations ($S_w = 21\% - 100\%$).

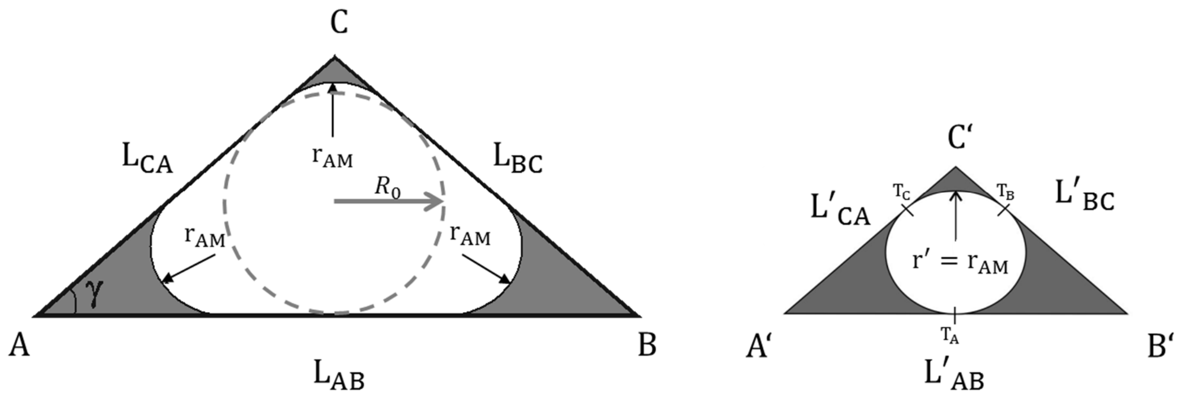

a) b)

Figure 3. Cross-sections of a partially saturated triangular tube. Arc meniscus of radius r_{AM} separates invading non-wetting phase (white) from adsorbed wetting phase (gray). a) Original triangle *ABC* with side lengths $L_{\mathrm{AB},}$ $L_{\mathrm{BC},}$ L_{CA}, and radius R_0 of its inscribing circle. b) Reduced triangle $A'B'C'$ of similar geometry. The wetting phase resides in the three corners (gray) with $r' = r_{\mathrm{AM}}$ being the radius of both the three interface arc menisci of *ABC* and of the inscribing circle of $A'B'C'$

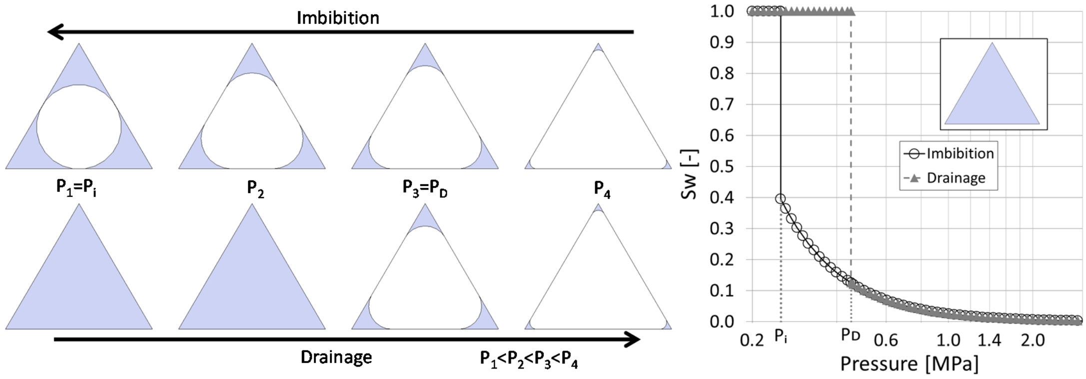

a) b)

Figure 4. a) Modeled distribution of water (gray) and gas (white) phases in an equilateral triangular tube with a side length of 1 μm during imbibition (top) and drainage (bottom). b) Water saturation versus capillary pressure during imbibition (○) and drainage (▲).

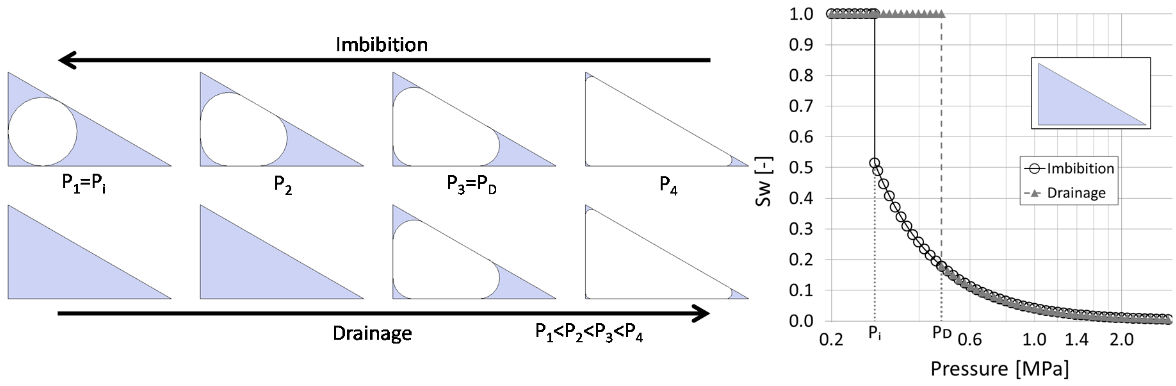

a) b)

Figure 5. a) Modeled distribution of water (gray) and gas (white) phases in a right-angled triangular capillary (G = 0.39) with side lengths $L = 1, 0.81, 0.58$ μm, and perimeter $P =$ 2.39 μm during imbibition (top) and drainage (bottom). b) Water saturation versus capillary pressure during imbibition (○) and drainage (▲).

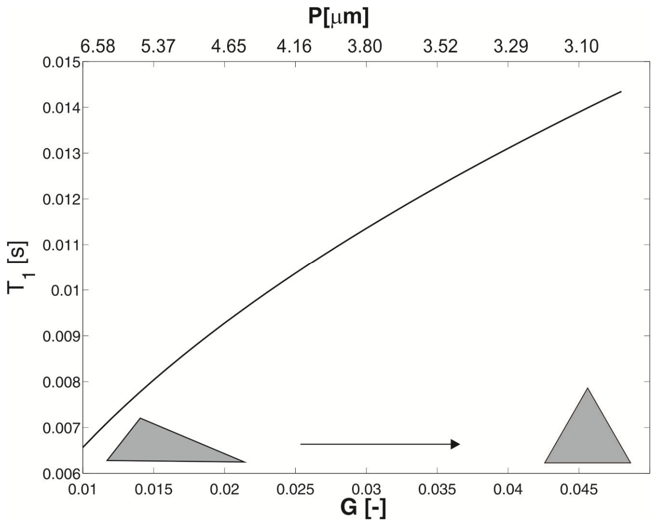

Figure 6. Longitudinal relaxation times T_1 of fully saturated triangular pores with constant cross-sectional area $A = 4.33 \cdot 10^{-13}$ m² versus shape factor $G = \frac{A}{P^2}$ and perimeter P. NMR parameters: $\rho_s = 10\ \mu m/s, T_{1\mathrm{B}} = 3\ s$.

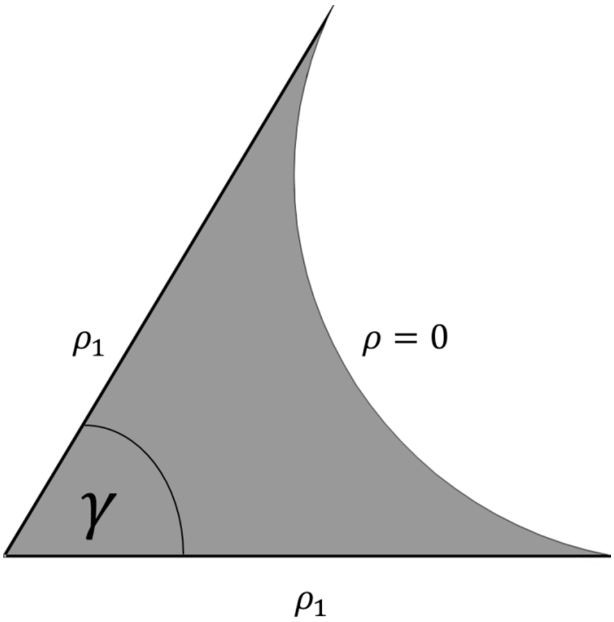

Figure 7. Saturated corner with active boundaries, i.e., $\rho_s = \rho_1 > 0$ at the corner's perimeter P_γ and a passive boundary at the air-water interface (meniscus), i.e., $\rho_s = \rho = 0$.

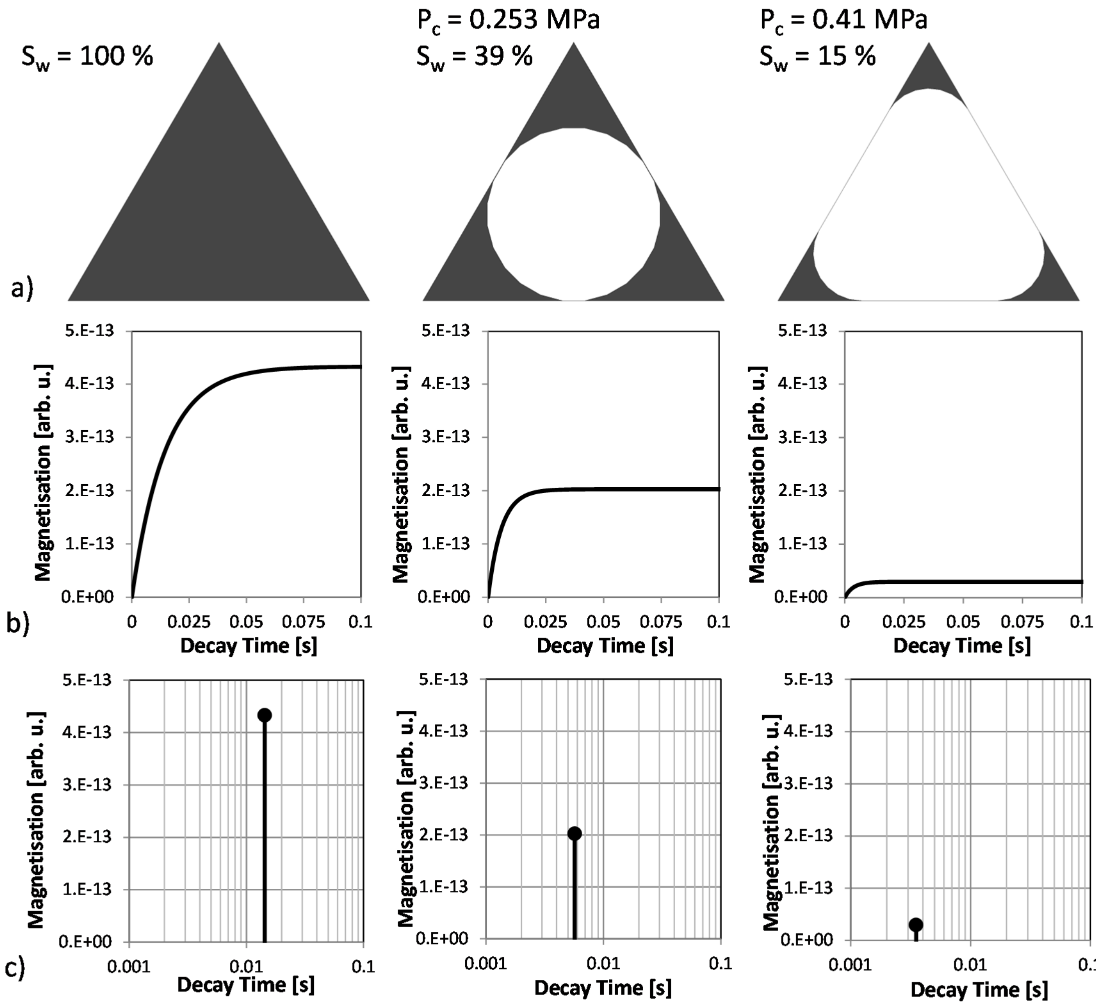

Figure 8. Water (black) and air (white) distributions within a triangular pore $(A_0 = 4.33 \cdot 10^{-13}\ \mathrm{m}^2,\ \rho_s = 10\ \mu\mathrm{m/s})$ at different capillary pressures for imbibition (a) with corresponding evolution of the (longitudinal) magnetization (b) and NMR T_1 relaxation times (c).

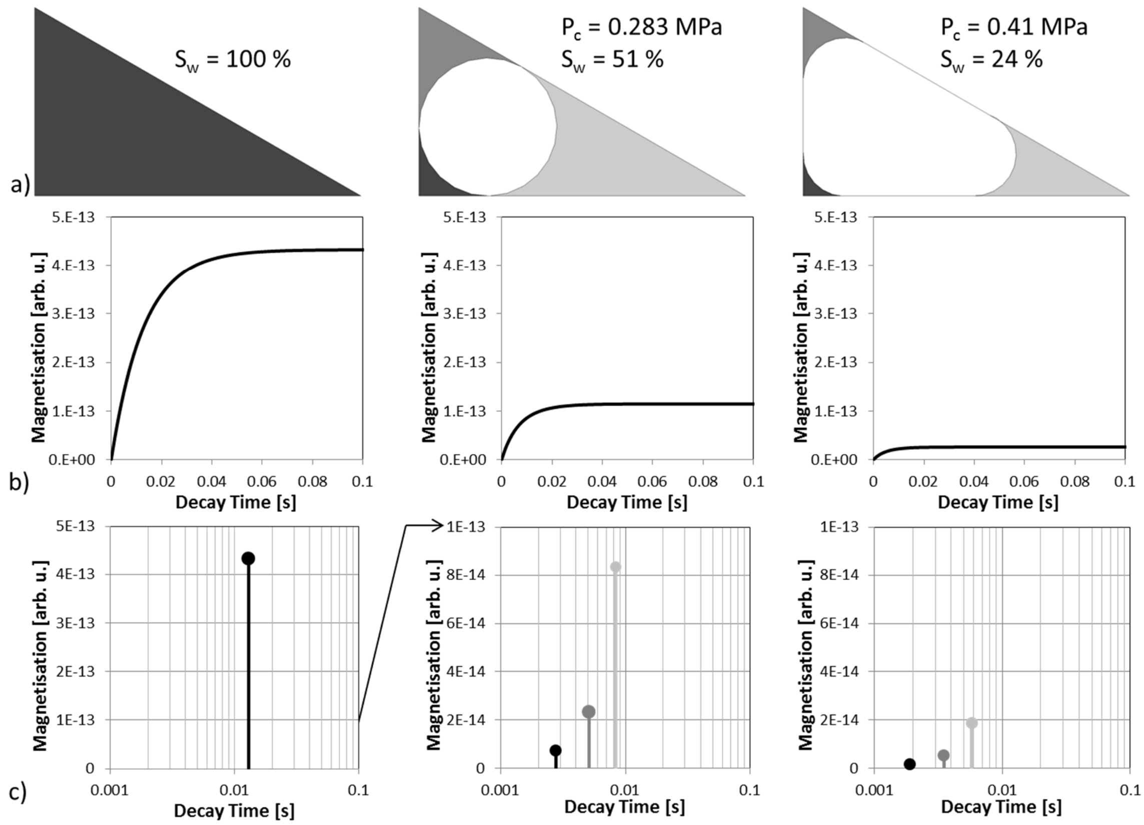

Figure 9. Water (black and grays) and air (white) distributions within a right-angled triangular pore ($A_0 = 4.33 \cdot 10^{-13}$ m^2, $\rho_s = 10\ \mu$m s^{-1}) at different capillary pressures for imbibition (a) with corresponding evolution of the (longitudinal) magnetization (b) and NMR T_1 relaxation times (c).

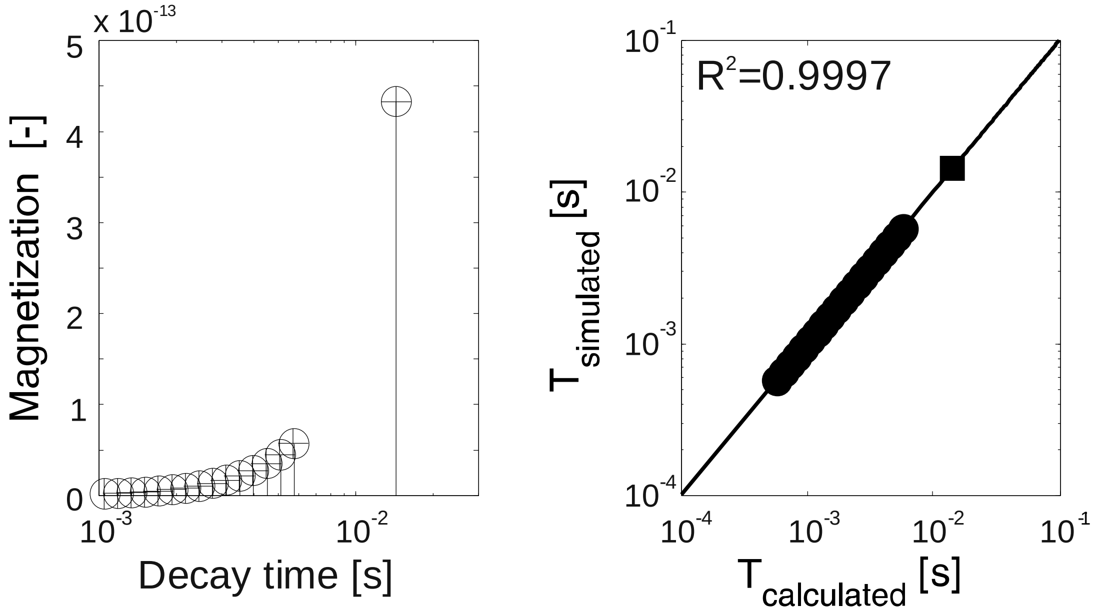

a) b)

Figure 10. NMR response of an equilateral triangular capillary pore model (with a side length of 1 μm). a) Magnetization versus T_1 decay time data of numerical (○) and analytical solutions (+) for all applied pressure levels. b) Cross-plot of numerically simulated and analytically calculated longitudinal T_1 decay times at partial (●) and full water saturation (■). A corresponding water saturation versus capillary pressure diagram is shown in Fig. 4.

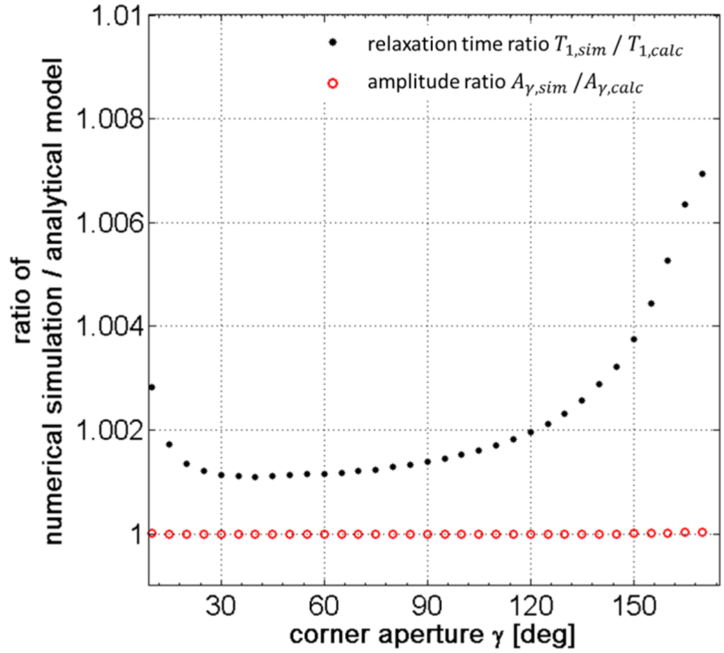

Figure 11. Comparison of analytical and calculated NMR relaxometry data originating from saturated pore corners (e.g. see Fig. 7) of varying apertures ($5° < \gamma < 175°$) and equal active surface-to-volume ratio $\frac{P_{\gamma_i}}{A_{\gamma_i}} = const.$ (NMR model parameters; $T_{1B} = 3$s, $D = 2.5\ 10^{-9}$ $m^2\ s^{-1}$, $\rho_s = 10\ \mu m\ s^{-1}$).

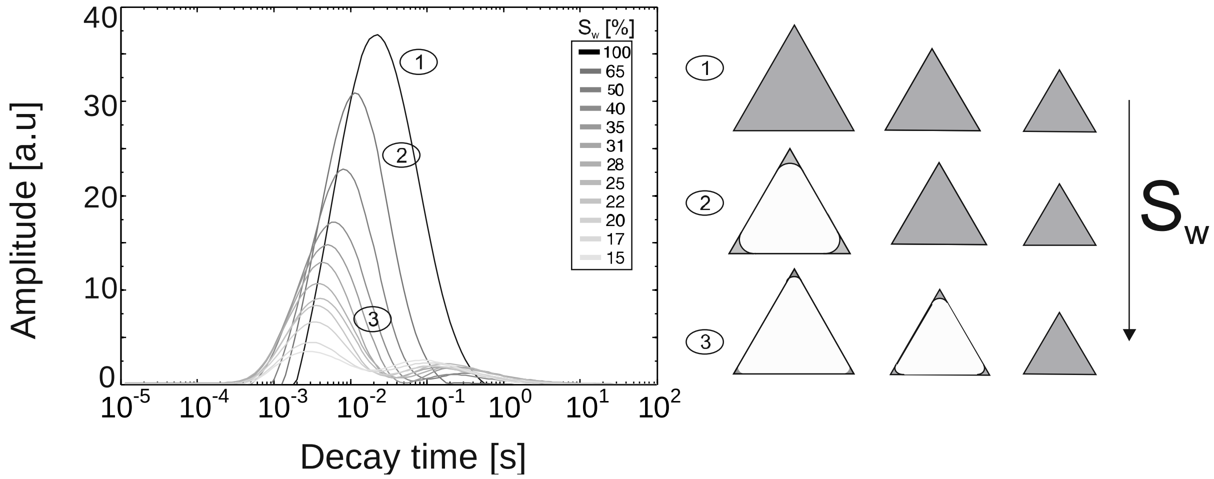

a) b)

Figure 12. a) NMR decay time distributions at different water saturation levels for a pore distribution of equilateral triangles. b) Concept sketch of saturated (gray) and de-saturated triangular capillaries for increasing pressure levels (1), (2) and (3), e.g., during drainage.

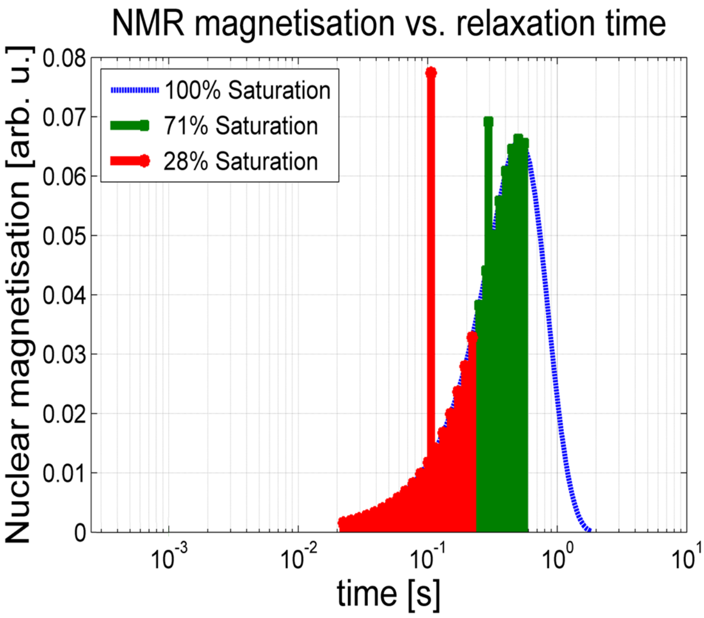

Figure 13: Relaxation components of fully (blue line) and partially de-saturated triangular pore size distribution. At a specific saturation level all pore corners with residual saturation exhibit the same NMR magnetization and relaxation behavior, thus superposing to a single fast relaxation component (e.g. red and green bars)

514

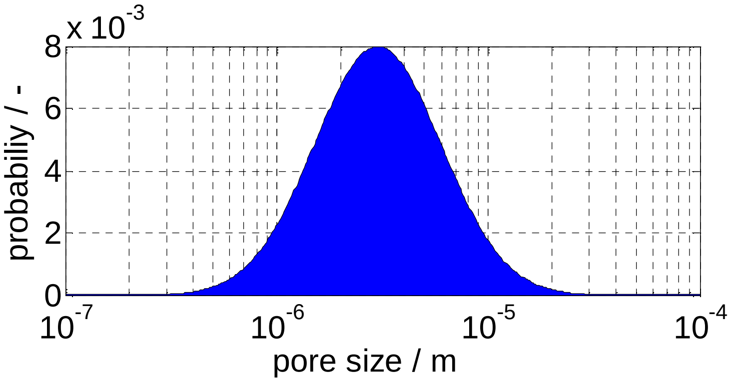

Figure 14. Pore-size distribution model (log-normal distribution: $\sigma = 0.3$ $\mu = 3 \cdot 10^{-6} m$) in analogy to that of the Rotliegend Sandstone shown in Fig. 2.

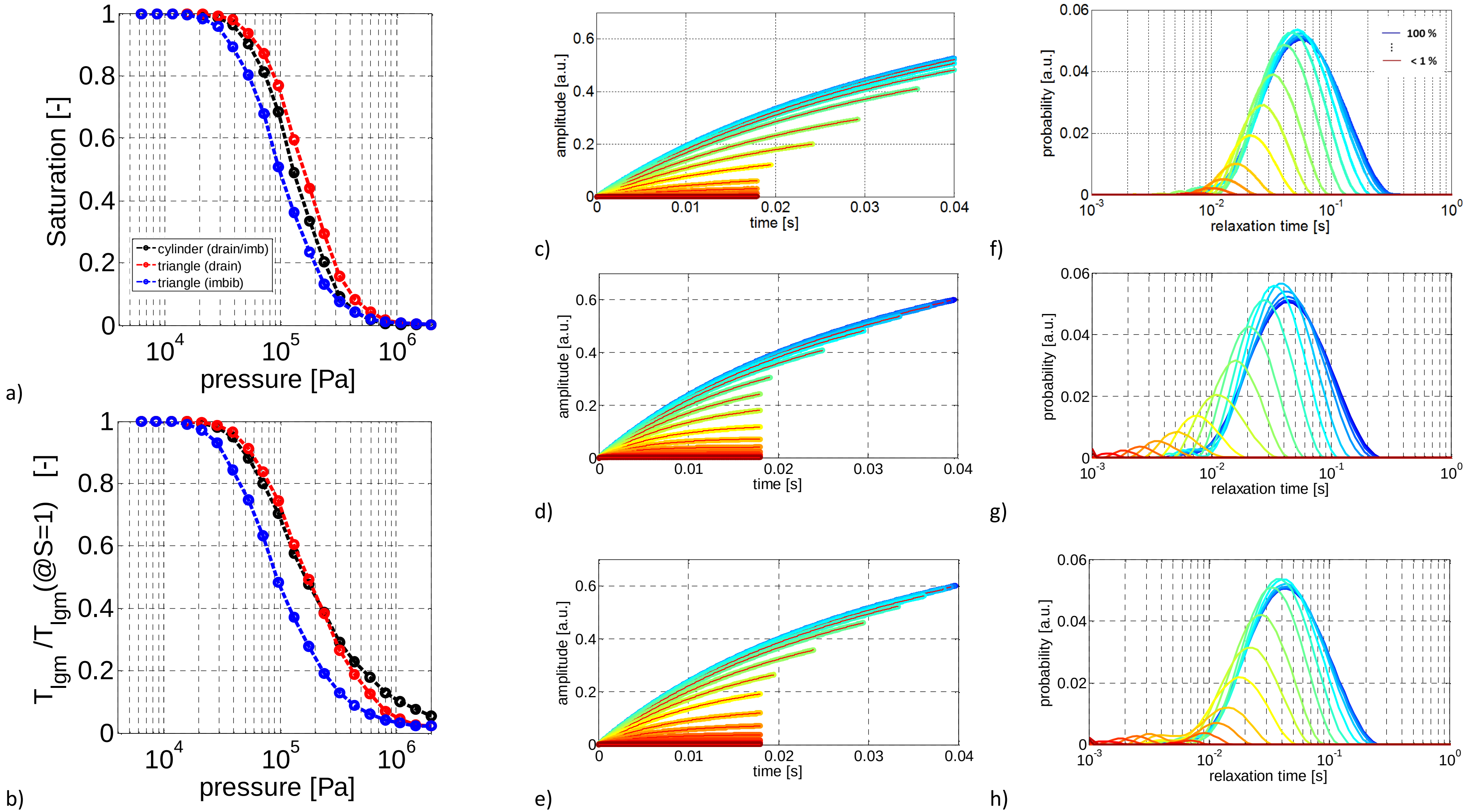

Figure 15: a) Modeled drainage and imbibition curves for circular and equilateral triangular capillary ensemble (cf Figure 14) and b) Corresponding normalized mean NMR T_1 relaxation times vs pressure curves. Modeled and fitted (red lines) NMR transient signals (longitudinal magnetization evolution) corresponding inverted NMR T_1 relaxation time distributions for 20 fully and partially saturated pore-size distributions ranging from < 1 % to 100 % saturation using circular (c, f) and equilateral triangular capillaries during imbibition (d, g) and drainage (e, h).